

# Topological Insights into Mutant Huntingtin Exon 1 and PolyQ Aggregates by Cryo-Electron Tomography

Jesus Galaz-Montoya (✉ [jgalaz@gmail.com](mailto:jgalaz@gmail.com))

Stanford University <https://orcid.org/0000-0002-0113-9325>

Sarah Shahmoradian

Laboratory of Biomolecular Research, Paul Scherrer Institute

Koning Shen

Stanford University

Judith Frydman

Stanford University <https://orcid.org/0000-0003-2302-6943>

Wah Chiu

Stanford University <https://orcid.org/0000-0002-8910-3078>

---

## Article

**Keywords:** HD, mHTT, CS, EMAN2

**Posted Date:** December 21st, 2020

**DOI:** <https://doi.org/10.21203/rs.3.rs-125810/v1>

**License:**   This work is licensed under a Creative Commons Attribution 4.0 International License.

[Read Full License](#)

---

**Version of Record:** A version of this preprint was published at Communications Biology on July 8th, 2021. See the published version at <https://doi.org/10.1038/s42003-021-02360-2>.

1 **Topological Insights into Mutant Huntingtin Exon 1 and PolyQ Aggregates by**  
2 **Cryo-Electron Tomography**

3 Jesús G. Galaz-Montoya<sup>1‡</sup>, Sarah H. Shahmoradian<sup>2\*</sup>, Koning Shen<sup>3\*†</sup>, Judith  
4 Frydman<sup>3</sup>, Wah Chiu<sup>1,4‡</sup>

5 <sup>1</sup> Department of Bioengineering and James H. Clark Center, Stanford University,  
6 Stanford, CA 94305, United States of America

7 <sup>2</sup> Department of Biology and Chemistry, Laboratory of Biomolecular Research, Paul  
8 Scherrer Institute, Villigen, Switzerland

9 <sup>3</sup> Department of Biology, Stanford University, Stanford, CA 94305, United States of  
10 America

11 <sup>4</sup> Division of CryoEM and Bioimaging, SSRL, SLAC National Accelerator Laboratory,  
12 Menlo Park, CA 94025, United States of America

13  
14 \* Equal contribution

15 † Current address: Department of Molecular and Cell biology, University of California,  
16 Berkeley, CA 94720, United States

17 ‡ Correspondence to: Jesús G. Galaz-Montoya, e-mail: jgalaz@gmail.com; Wah Chiu,  
18 e-mail: wahc@stanford.edu

22 **ABSTRACT**

23           Huntington disease (HD) is a neurodegenerative trinucleotide repeat disorder  
24 caused by an expanded poly-glutamine (polyQ) tract in the mutant huntingtin (mHTT)  
25 protein. The formation and topology of filamentous mHTT inclusions in the brain  
26 (hallmarks of HD implicated in neurotoxicity) remain elusive. Using cryo-electron  
27 tomography and subtomogram averaging, here we show that mHTT exon 1 and polyQ-  
28 only aggregates *in vitro* are structurally heterogenous and filamentous, similar to prior  
29 observations with other methods. Yet, we find filaments in both types of aggregates under  
30 ~2 nm in width, thinner than previously reported, and regions forming large sheets. In  
31 addition, our data show a prevalent subpopulation of filaments exhibiting a lumpy slab  
32 morphology in both aggregates, supportive of the polyQ core model. This provides a basis  
33 for future cryoET studies of various aggregated mHTT and polyQ constructs to improve  
34 their structure-based modeling as well as their identification in cells without fusion tags.

35

36

37

38

39

40

41

42

## 43 INTRODUCTION

44           Huntington disease (HD) is a neurodegenerative, fatal trinucleotide repeat  
45 disorder caused by a polyQ expansion in exon 1 of mutant huntingtin (mHTT) exceeding  
46 a pathogenic threshold of  $Q > \sim 35$ <sup>1</sup>. Patients suffer from motor and cognitive impairments  
47 and despite our increased understanding of HD<sup>2</sup> and promising clinical trials<sup>3</sup>, cures and  
48 preventive treatments remain elusive<sup>4</sup>.

49           Expression of mHTT exon 1 (a caspase cleavage product within cells, hereafter  
50 “mEx1”) elicits HD phenotypes in cellular and animal models<sup>5-8</sup>, including primates<sup>9</sup>.  
51 Furthermore, mEx1 inclusions in mouse and human brains<sup>10,11</sup> are morphologically similar  
52 to those in R6/2 and mEx1 knock-in mice<sup>12</sup>.

53           A polyQ expansion in different genes causes at least eight other disorders with a  
54 similar pathogenic Q-repeat length threshold, irrespective of flanking motifs<sup>13,14</sup>, and  
55 polyQ peptides as short as  $Q=20$  are toxic when they contain a nuclear localization  
56 signal<sup>15</sup>. Since structure often determines function<sup>16</sup>, as shown for mHTT toxic  
57 aggregates<sup>17,18</sup>, an increased structural understanding of polyQ aggregates can help  
58 uncover the mechanisms underlying their biogenesis, development, and cytotoxicity to  
59 better model polyQ disorders.

60           Both small mHTT oligomers and large inclusion bodies (IBs) can be neurotoxic<sup>19,20</sup>.  
61 Filamentous aggregates of mEx1 constructs with various polyQ lengths (mEx1-Q<sub>n</sub>) have  
62 been amply visualized with negative staining transmission electron microscopy (NS-  
63 TEM)<sup>21-23</sup>, a technique often limited to 2D projections and subject to metal stain and drying  
64 artifacts. Two recent studies used cryo focused ion beam milling and electron tomography  
65 (cryoFIB-ET) to visualize transfected mEx1-Q97 forming IBs within yeast<sup>24</sup> and HeLa<sup>25</sup>

66 cells. However, a green fluorescence protein (GFP) fusion tag was used, which can alter  
67 mEx1 aggregation<sup>26</sup>.

68 Here, we used direct observation (without heavy metal stain or fusion tags) by  
69 cryo-electron tomography (cryoET) and subtomogram averaging (STA)<sup>27,28</sup> to visualize  
70 vitrified filamentous mEx1-Q51 and Q51 (a peptide consisting of only glutamines)  
71 aggregates *in vitro*. We leveraged our initial observations of mEx1-Q51 filaments by  
72 cryoET<sup>29-31</sup> and capitalized on recent algorithmic developments including compressed  
73 sensing for tomographic reconstruction<sup>32,33</sup>, convolutional neural networks for feature  
74 annotation<sup>34</sup>, and automated fiducial-less tiltseries alignment and subtiltseries refinement  
75 for subtomogram averaging<sup>35</sup> to resolve previously unattainable structures. Our study  
76 provides a three-dimensional (3D), nanometer-resolution structural description of  
77 untagged, vitrified mEx1 and Q-only aggregates, finding filaments that are thinner than  
78 previously observed, laminated sheets, and a predominant conformation exhibiting a  
79 lumpy slab morphology that supports the polyQ core model.

80

## 81 **RESULTS**

### 82 **Mutant huntingtin exon 1-Q51 filaments exhibit a large variation in width, narrow** 83 **branching angles, and lamination**

84 We analyzed tomographic tiltseries of vitrified mEx1-Q51 (**Figure 1a**), collected as  
85 previously described (see Methods)<sup>29</sup>. Owing to the higher contrast and minimized  
86 missing wedge artifacts attainable with compressed sensing (CS) compared to standard  
87 weighted back projection<sup>32</sup>, we incorporated CS in our pipeline to reconstruct the tiltseries

88 into tomograms (see Methods), which exhibited aggregated filamentous densities (**Figure**  
89 **1b,c**). While CS might introduce artifacts at high resolution in the subnanometer range, it  
90 has been demonstrated to produce faithful reconstructions at nanometer resolution<sup>36</sup>. The  
91 most frequently observed widths from aggregates in six tomograms ranged between ~5  
92 and ~16 nm, with the thinnest filaments exhibiting regions down to ~2 nm thickness  
93 (**Figure 1d,e**). On the other hand, the thickest filaments measured over ~20 nm in width.  
94 These measurements are not consistent with a cylindrical shape of a single radius, as  
95 reported in recent cryoFIB-ET studies<sup>24,25</sup>. Rather, our observations are consistent with a  
96 heterogeneous plethora of thin filaments, rectangular prisms, and even sheets of varying  
97 size. We interpret the predominant species among our observed filaments as 3D  
98 rectangular slabs, which could exhibit many different center-slice widths in between their  
99 widest and narrowest dimensions when sliced computationally at slanted angles. Our  
100 computational simulations of filamentous subtomograms using EMAN2<sup>37</sup> support this  
101 model (**Supplementary Figure S1**).

102 **Figure 1. MEx1-Q51 filaments**  
103 **exhibit a large variation in width**  
104 **within and across filaments. (a)**

105 Schematic of the mEx1-Q51  
106 construct. (b) Slice parallel to xy (~1.7  
107 nm thick) through a representative 4x  
108 down-sampled cryoET tomogram of  
109 aggregated mEx1-Q51, reconstructed

110 with compressed sensing, lightly  
111 filtered to enhance visualization, and

112 (c) corresponding semi-automated 3D  
113 annotation. (d) Selected areas from

114 slices of large mEx1-Q51 aggregates  
115 showing individual filaments, widely  
116 varying in width, with the thinnest  
117 filaments exhibiting regions down to  
118 ~2 nm width, indicated by the red

119 arrows. (e) Zoomed-in view of a xy

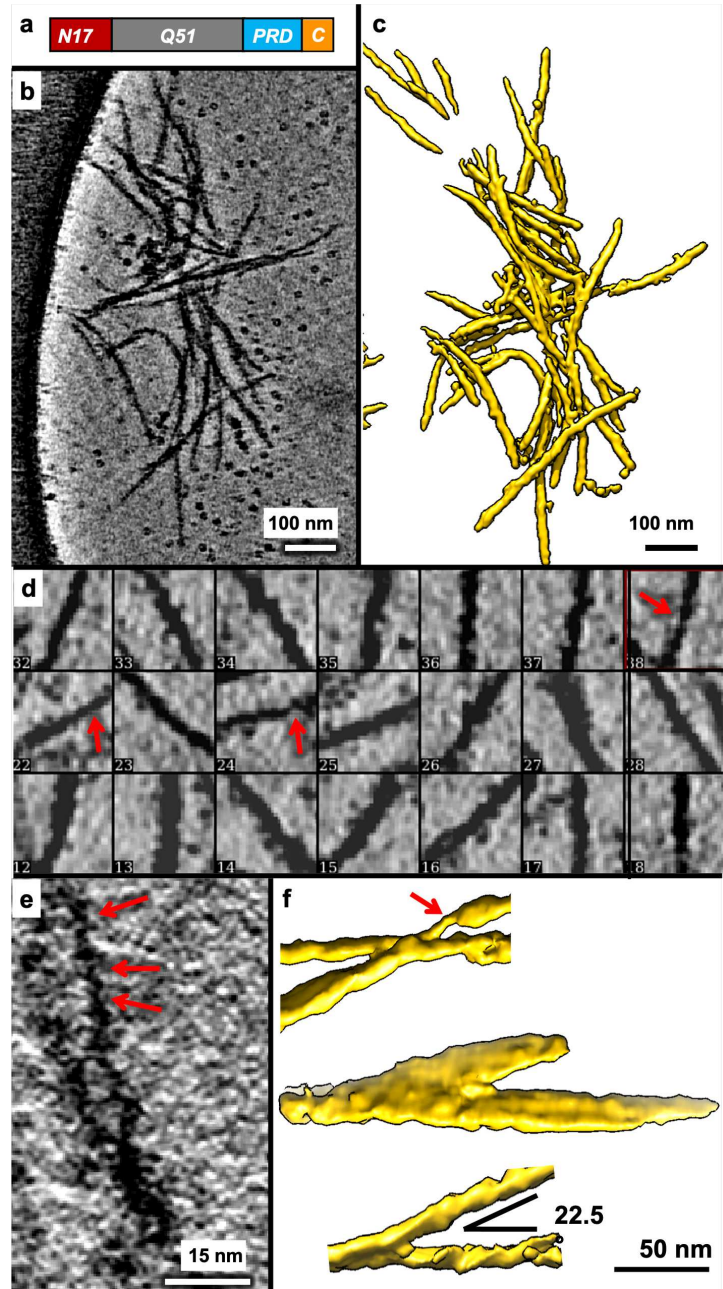
120 slice (~0.4 nm thick) from a selected region of a tomogram without any down-sampling,

121 showcasing ultra-thin regions in mEx1-Q51 filaments. (f) Sections of annotated mEX1-

122 Q51 filamentous aggregates from cryoET tomograms showing relatively narrow

123 branching angles and an example of a thicker laminated sheet-like region (the annotation

124 example in the middle).

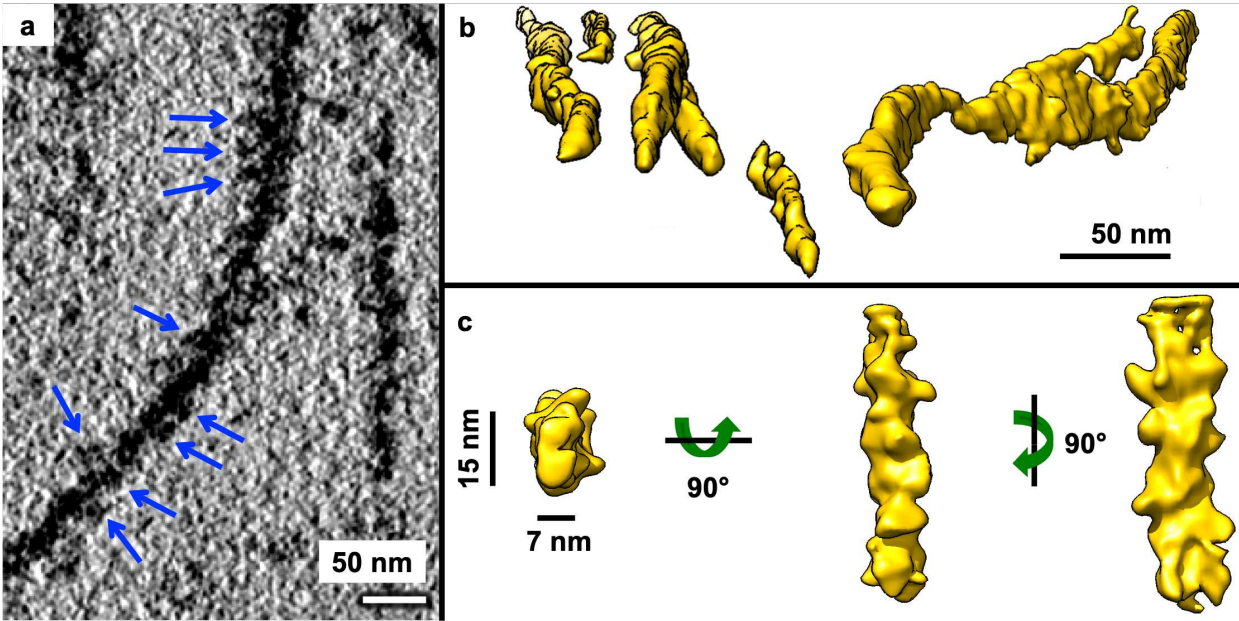


125

126 We used semi-automated annotation based on neural networks<sup>34</sup> to visualize in  
127 3D what kind of objects yielded the extensive width variations detectable in 2D slices of  
128 3D tomograms. Visualizing mEx1 filaments as 3D isosurfaces (**Figure 1C**;  
129 **Supplementary Figure S2**) revealed filaments of different dimensions altogether,  
130 including regions that appeared as sheets as thick as ~50 nm, estimated from the  
131 annotations and from their persistence through 2D slices. The mEx1 filaments seemed to  
132 predominantly branch out at angles varying from ~10° to ~45° (only sporadically larger),  
133 with angles between ~20° to ~25° being most common (**Figure 1f**).

#### 134 **Subpopulation of mEx1-Q51 filament segments exhibits a lumpy, slab-shaped** 135 **morphology**

136 Many filaments appeared to be lumpy both in 2D slices from 3D tomograms  
137 (**Figure 2a**) as well as in in 3D annotations (**Figure 2b**), suggestive of potential periodicity.  
138 Thus, we performed subtomogram averaging (STA) of filament segments, avoiding  
139 obviously-laminated regions and thick bundles. The subtomogram average of mEx1-Q51  
140 filament segments (n=450, from 6 tomograms) converged to a lumpy ~7x15 nm slab at  
141 ~3.5 nm resolution (**Figure 2c**). The Fourier transform of 2D re-projections of the average  
142 did not reveal crisp layer lines, in agreement with previous studies suggesting that mEx1  
143 filaments do not exhibit a canonical amyloid structure with parallel subunits stacked  
144 helically in register<sup>22</sup>. Indeed, HD does not strictly fit among the diseases known as  
145 amyloidoses<sup>38</sup>; nonetheless, the power spectra showed bright maxima off of the meridian,  
146 at ~11.7 nm (**Supplementary Figure 4a**), suggestive of potential periodicity for at least  
147 relatively short stretches (~65 nm, the length included in the extracted subtomograms).



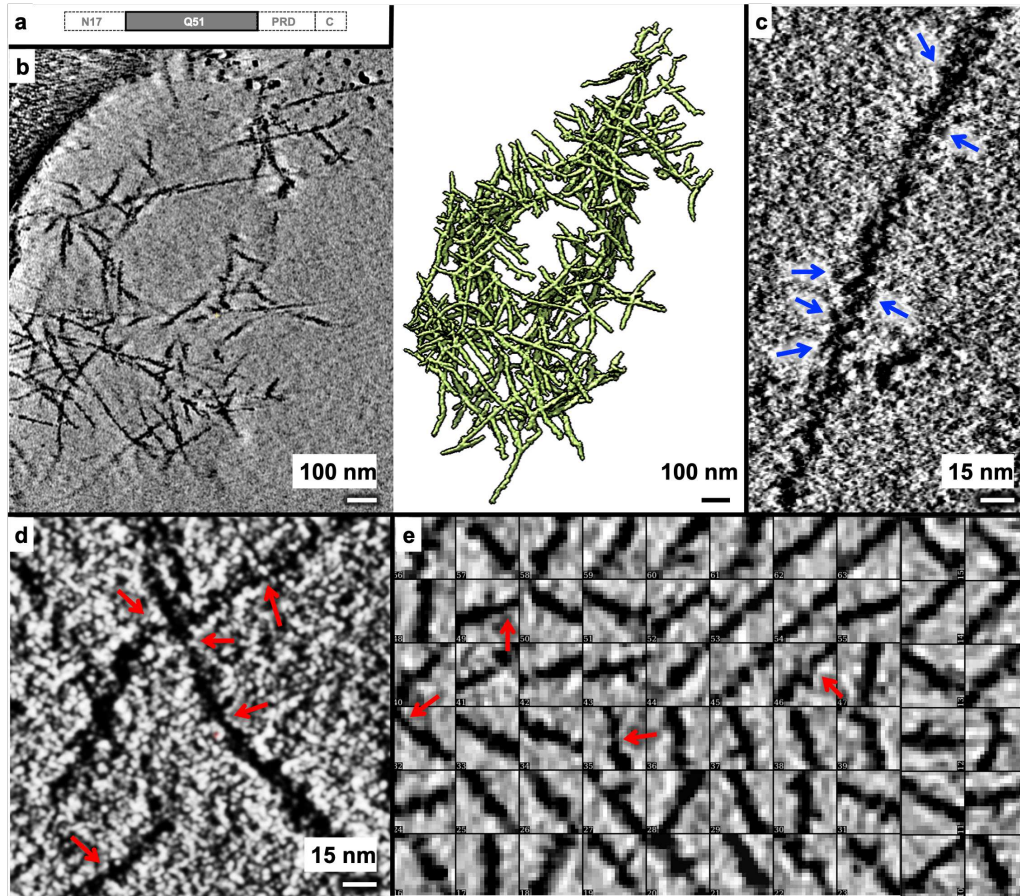
148

149 **Figure 2. Aggregated mEx1-Q51 exhibits lumpy, slab-shaped filaments.** (a) Pseudo-  
 150 periodic pattern of repeating lumps (blue arrows) along the length of an mEx1-Q51  
 151 filament as seen in an xy slice (4.4 Å thick) from a tomogram of aggregated mEx1-Q51.  
 152 (b) Selected regions from semi-automated neural network annotations showing lumpy  
 153 filaments of various widths, including sheet-like regions (middle region of right-most  
 154 example). (c) Subtomogram average of a subpopulation of filament segments exhibiting  
 155 a lumpy 7x15 nm slab-shaped morphology.

156

157 **Lumpy, slab-shaped Q51-only filaments also exhibit lamination**

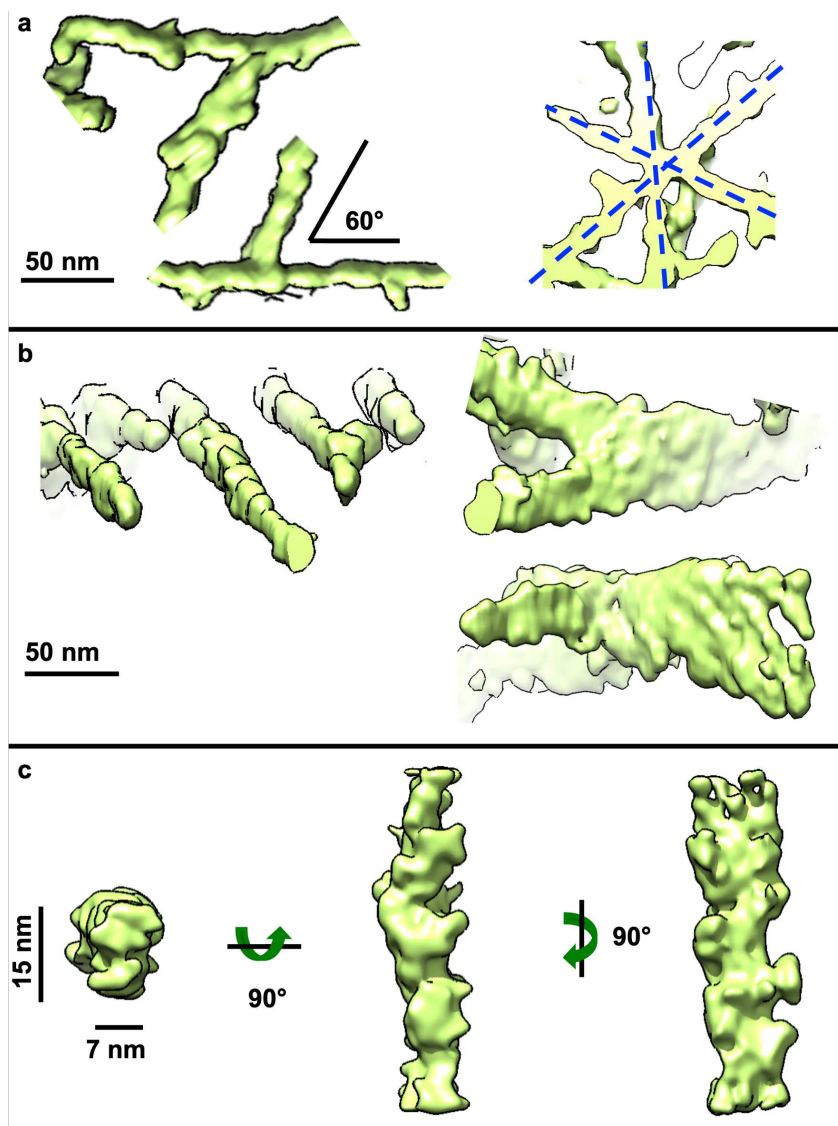
158 Since an expanded polyQ tract is the common culprit of all polyglutamine diseases,  
 159 we performed the same analyses for a Q51-only peptide (**Figure 3a**) as reported above  
 160 for mEx1-Q51. We found that Q51 also forms aggregates (**Figure 3b, Supplementary**  
 161 **Figure 3**) exhibiting lumpy filaments (**Figure 3c**) of varying widths (**Figure 3d,e**), with  
 162 regions as thin as ~2 nm.



163

164 **Figure 3. Lumpy Q51 filaments exhibit a large range of widths.** (a) Schematic of the  
 165 Q51 construct, lacking all mEx1 domains except for the polyQ tract. (b) Slice parallel to  
 166 the xy plane (~2.1 nm thick) through a representative 4x down-sampled cryoET tomogram  
 167 of aggregated Q51 reconstructed with compressed sensing (left) and corresponding 3D  
 168 annotation (right). Zoomed-in views of xy slices (~0.5 nm thick) from selected regions of  
 169 the tomogram shown in A but without any down-sampling, exhibiting (c) a pseudo-  
 170 periodic pattern of repeating lumps along the length of a Q51 filament (blue arrows), and  
 171 (d) regions in thin filaments that are as thin as ~2 nm in width (red arrows). (e) Examples  
 172 of 2D xy slices through representative 3D subtomograms of Q51 filaments showing a  
 173 wide variation in width, including super-thin regions ~2 nm in width (red arrows).

174 **Figure 4. Aggregated Q51 exhibits lamination sheets and predominantly lumpy,**



**slab-shaped filaments. (a)** Representative sections of annotated Q51 filamentous aggregates from cryoET tomograms showing their most common branching/crossover angle ( $\sim 60^\circ$ ), often in an asterisk-like pattern, and **(b)** thicker regions (right) akin to lamination, alongside thinner ones (left). **(c)** Subtomogram average of a subpopulation of filament segments exhibiting a lumpy 7x15 nm slab-shaped morphology.

191

192 Q51 filaments branched out/crossed over more often and at wider angles than  
193 mEx1-Q51 filaments, with  $\sim 60^\circ$  being the most common angle (**Figure 4a**). Furthermore,  
194 Q51 filaments exhibited larger lamination sheets than those of mEx1-Q51 of up to  $\sim 60+$   
195 nm in width (**Figure 4b**). The subtomogram average of non-laminated filament segments  
196 ( $n=493$ , from 6 tomograms) converged to  $\sim 3.2$  nm resolution and also revealed a lumpy

197 ~7x15 nm slab (**Figure 4c**), with a crossover length of ~11.2 nm according to the power  
198 spectrum of its projections (**Supplementary Figure 4b**), all strikingly similar results to  
199 those obtained for mEx1-Q51.

200

## 201 **DISCUSSION**

202 In one of the earliest reports visualizing mEx1-Q51 filamentous aggregates by NS-  
203 TEM, filaments digested with factor Xa or trypsin, which removes mEx1's N17 domain  
204 critical to mHTT localization and function<sup>39</sup>, were reported to have a diameter of ~7.7-12  
205 nm from 2-dimensional (2D) images<sup>40</sup>. These were occasionally referred to as ribbons,  
206 and other 2D NS-TEM observations have reported similar filaments with a 10-12 nm  
207 diameter, which may associate laterally<sup>22</sup>. However, apparent lateral associations in 2D  
208 NS-TEM observations may arise from the compression of all densities into a single layer  
209 due to dehydration. In contrast, the vitrified filaments seen in our 3-dimensional (3D)  
210 tomograms varied much more in width within and across filaments, similar to those  
211 reported in studies visualizing aggregated Q-only peptides with NS-TEM<sup>41,42</sup>, which also  
212 detected wide ribbons and thin filaments under different incubation temperatures and  
213 using a freeze-concentration method involving cycles of freezing and thawing. Here, our  
214 observations did not suffer from NS-TEM artifacts and were conducted at 30° C, without  
215 special temperature manipulations.

216 While other amyloidogenic filaments have been amply studied using cryo electron  
217 microscopy (cryoEM)<sup>43-50</sup>, cryoEM studies of mHTT and polyQ-containing aggregates  
218 have been extremely scant in comparison, likely due to the extensive conformational  
219 heterogeneity of these specimens<sup>51</sup>, which limits the applicability of bulk techniques (*e.g.*,

220 Circular Dichroism) and calls for the increasing application of single molecule  
221 techniques<sup>52</sup>. Single molecule techniques such as Atomic Force Microscopy (AFM) and  
222 various modalities of electron microscopy (EM) can observe individual components in  
223 aggregates (molecules, oligomers, filaments). For EM-related methods, these  
224 components can be classified prior to averaging. Of note, cryoET is the most suitable  
225 method to investigate the overall structure of relatively large and thick, hydrated samples  
226 exhibiting extensive conformational and compositional heterogeneity as it avoids  
227 adsorption of the specimen onto 2D surfaces and the confounding effect of potentially  
228 overlapping densities from different components, as in 2D projections produced by single  
229 particle cryoEM.

230 In two recent cryoFIB-ET studies, mEx1-Q97-GFP filaments were observed and  
231 annotated in transfected cellular systems but were not averaged. Rather, they were either  
232 modeled as cylinders with an 8-nm diameter for template-based annotation<sup>25</sup> or were  
233 segmented as 16 nm filaments<sup>24</sup>, surprisingly twice as thick in the latter study than in the  
234 former, perhaps owing to differences in the non-native expression systems used or to the  
235 confounding presence of GFP fusion tags. Indeed, there can be caveats to using fusions  
236 to fluorescent proteins as tags, from impairing the viability and growth of cells via toxic  
237 effects from tag aggregation, excitation, or photoactivation, to changing the structure,  
238 function, and cellular localization of the tagged protein<sup>53</sup>. Template-based approaches  
239 have been successfully applied to annotate more regularly-shaped biological  
240 filaments<sup>54,55</sup>; however, our data here suggest that the use of a cylindrical template is not  
241 an adequate approach to annotate widely heterogeneous mEx1 and polyQ aggregates  
242 with filamentous densities of varying dimensions. Indeed, when identifying features in

243 tomograms, template matching can be biased<sup>56</sup> and manual human annotation is  
244 subjective and therefore often uncertain and inconsistent<sup>57</sup>. On the other hand, here we  
245 used template-free, semi-automated annotation based on machine learning since it can  
246 ameliorate these issues by minimizing human input and the use of *a priori* constraints  
247 inherent in templates<sup>34</sup>.

248         A recent atomic force microscopy (AFM) study on mEx1-Q49 aggregation  
249 suggested that nucleated branching from filaments, rather than lateral associations  
250 among them, leads to large bundles<sup>58</sup>. However, branching does not explain how the  
251 thinner (< 2 nm thick) filaments that we observe here would assemble into thicker slabs  
252 and sheets without associating laterally or growing transversally to the main filament axis.  
253 Rather, our results suggest that preformed thin filaments can associate laterally and/or  
254 that growing filaments can expand transversally in addition to longitudinally, akin to the  
255 lamination observed for A $\beta$ <sup>59</sup>, for both mEx1-Q51 and Q51.

256         While AFM is limited to ~30 nm in lateral resolution of surface measurements of  
257 specimens that are often absorbed and dried onto a 2D substrate, an earlier AFM study  
258 of aggregated Q44 peptide detected regions in filament tips with a “height” (the size of  
259 the specimen in the direction perpendicular to the adsorption surface) as thin as ~5 nm<sup>60</sup>.  
260 This and the thinness of some of the filament regions we observed here (as thin as ~2  
261 nm) seem to disagree with the minimum width of ~7-8 nm proposed for polyQ filaments  
262 from various Qn constructs in a prior NMR study that also presented NS-TEM images<sup>61</sup>.  
263 However, the latter study reports filament widths for a Q54 peptide from NS-STEM  
264 images from ~7-8 nm up to ~16 nm, in striking agreement with the short and long sides

265 of the slab-shaped model we propose here as the predominant morphology for filaments  
266 formed by both mEx1-Q51 and Q51.

267 The morphological characteristics deviating from thin cylindrical shapes to form  
268 lumpy slabs and sheets may serve as a structural hallmark to identify untagged mHTT  
269 aggregates in cells. Furthermore, the more frequent and wider-angle branching of Q-only  
270 filaments compared to mEx1 is consistent with our prior 2D cryoEM observations<sup>31</sup>,  
271 suggesting that the N17 domain promotes inter-filament bundling. Conversely, the  
272 occurrence of branching might be primarily polyQ-driven. Indeed, our 3D observations  
273 here, which are free from fusion tags, stains, dehydration, flattening, and crystallization  
274 artifacts, provide a transforming complement and clarification to previous studies by NS-  
275 TEM and AFM, as well as light microscopy<sup>62,63</sup>, which visualized mEx1 filamentous  
276 aggregates at a coarser level: features often described as globules or oligomers or thick  
277 filaments actually correspond to bundles of many interwoven thinner filamentous  
278 densities when viewed by cryoET.

279 The fact that the predominant populations for both mEx1 and Q-only filaments  
280 exhibit a similar lumpy slab shape and distance between putative crossovers as revealed  
281 by subtomogram averaging suggests that the morphology of their core is dictated by and  
282 primarily comprised of the polyQ tract, and that the flanking domains in mEx1 are largely  
283 exposed at the filament surface, allowing them to modulate inter-filament aggregation.  
284 This interpretation agrees with previous nuclear magnetic resonance (NMR) studies on  
285 non-pathogenic<sup>64</sup> and pathogenic<sup>65,66</sup> mEx1 variants that propose the existence a dense  
286 polyQ core.

287 In one of the latest studies supporting the polyQ-core model<sup>67</sup>, the authors  
288 observed mEx1-Q44 filaments formed at two different temperatures by 2D NS-TEM  
289 images (presented in the supplement). The widths reported for these filaments were ~6.5  
290 nm and ~15.2 nm, in striking agreement with the dimensions of our slab-shaped  
291 subtomogram averages of filament segments from 3D cryoET tomograms of vitrified  
292 mEX-Q51 and Q51. While their hypothesis that the thicker ~15.2 nm filaments must arise  
293 from two interwinding protofilaments ~6.5 nm thick seems to be compatible with our  
294 observations here, their model proposing that the flanking domains mediate such  
295 interwinding does not explain our observation that polyQ-only filaments also yield a  
296 dominant subpopulation with the same ~7x15 nm slab morphology, which could also  
297 correspond to two interwoven protofilaments without flanking domains to bind them. If,  
298 indeed, the mEx1-Q51 and Q51-only predominant subpopulations of ~7x15 nm filaments  
299 are composed of two thinner interwinding protofilaments, our data suggest that they might  
300 be bound primarily via polyQ-polyQ interactions.

301 Our observations here warrant further cryoET experiments with much larger  
302 datasets of aggregation-competent mEx1 and polyQ-only constructs devoid of  
303 solubilization and purification tags, as even these can cause modest alterations in  
304 aggregation kinetics<sup>68,69</sup>. Datasets at higher magnification and contrast, using state-of-  
305 the-art instrumentation, could test whether there exist filament species even thinner than  
306 the ~2 nm regions we observed here, as could probe the effects of increasing polyQ  
307 length on the 3D morphologies of vitrified filamentous aggregates. Assessing the effects  
308 of post-translational modifications (PTMs) on filament and overall aggregate structure  
309 with cryoET might be of particular significance, as some PTMs modulate aggregation with

310 neuroprotective effects<sup>70</sup>. Finally, sonication concomitant with trypsin digestion of mEx1  
311 filaments might yield a homogenous-enough population of the polyQ core that may be  
312 more amenable to higher-resolution cryoEM/ET studies.

313

## 314 **METHODS**

### 315 ***In vitro* mEx1-Q51 and Q51 peptide aggregation assays and cryoET sample** 316 **preparation**

317 We used mutant huntingtin (mHTT) exon 1 with 51 glutamine repeats (mEx1-Q51)  
318 and a polyQ-only peptide with 51 repeats (Q51), each of them fused to a TEV cleavage  
319 sequence and a GST tag, as previously described<sup>31</sup>. Aggregation was initiated separately  
320 at a concentration of 6  $\mu$ M for each construct *in vitro* by addition of AcTEV<sup>TM</sup> protease  
321 (Invitrogen), as previously described for mEx1-Q51<sup>29</sup>. The samples were incubated at 30  
322 °C before vitrification. Aliquots of 2.5  $\mu$ m were separately applied to 200-mesh holey  
323 carbon Quantifoil copper grids (previously washed with acetone, and rinsed in PBS)  
324 between 4 and 6 h post-initiation of aggregation. The grids were plunge-frozen in a liquid  
325 ethane bath kept at liquid nitrogen temperature using a Vitrobot Mark III (FEI Instruments).

### 326 **Tiltseries collection**

327 We collected six tiltseries of the Q51 peptide using SerialEM software<sup>71</sup> on a  
328 JEM2100 electron microscope operated at 200 kV from -60° to 60° in 2° increments, at 6  
329  $\mu$ m target underfocus, 5.29 Å/pixel sampling size, with a cumulative dose of  $\sim$ 80 e/Å<sup>2</sup>. We  
330 also reanalyzed a previous dataset comprised of 20 tiltseries of mEx1-Q51 + TRiC,

331 collected similarly to the Q51 peptide dataset, as previously described<sup>29</sup>, with a slightly  
332 finer sampling size of 4.4 Å/pixel.

### 333 **Tomographic reconstruction**

334 All mEx1-Q51 and Q51 tilt series were binned by 2x and initially aligned and  
335 reconstructed into tomograms with IMOD<sup>72</sup>. Images with artifacts (grid bars in the field of  
336 view blocking large regions of the specimen, evident large drift, obvious radiation  
337 damage, etc.) were manually removed prior to tiltseries alignment and tomographic  
338 reconstruction with weighted back projection. After assessing sample thickness, the  
339 tiltseries were reconstructed again into tomograms using compressed sensing (CS) as  
340 implemented in ICON-GPU<sup>32,33</sup> to improve contrast. Of note, CS also partially restores  
341 information that is lacking due to the missing wedge artifact inherent in all conventional  
342 single-axis limited-angle tomography experiments, such as conventional cryoET<sup>73</sup>. The  
343 tiltseries were aligned and reconstructed yet a third time for subtomogram averaging  
344 purposes (as described below), using a new pipeline for cryoET in EMAN2<sup>35</sup> that performs  
345 sub-tiltseries refinement, akin to prior hybrid methods combining concepts from single  
346 particle analysis cryoEM and subtomogram averaging<sup>74-76</sup>. We processed the mEx1-Q51  
347 and Q51 datasets separately in virtually identical ways.

### 348 **Tomogram annotation**

349 Since the ultimate goal of the new EMAN2 cryoET pipeline<sup>35</sup> is to perform  
350 subtiltseries refinement for subtomogram averaging, tomogram quality only needs to be  
351 sufficient to allow for particle identification. Indeed, in EMAN2 not as many parameters  
352 are refined during tomographic reconstruction as compared to IMOD, often resulting in  
353 lower-quality tomograms. For this reason, we performed all tomographic annotations on

354 better-quality tomograms aligned with IMOD and reconstructed with CS, as described  
355 above. MEx1-Q51 and Q51 annotations were carried out on binned-by-4 tomograms  
356 using EMAN2's neural network semi-automated annotation tools<sup>34</sup>, except that ~2-3x as  
357 many references as the 10 recommended were segmented to seed annotation, and ~2-  
358 3x as many negative samples as the 100 recommended were selected to minimize false  
359 positives. We initially performed annotation of all mEx1-Q51 and Q51 tomograms by  
360 applying the convolutional neural network from the best tomogram to all the rest,  
361 separately for each specimen. However, false positives (such as annotating the carbon-  
362 hole edge and/or gold fiducials) were reduced further when we generated a neural  
363 network specific for each mEx1-Q51 and Q51 tomogram.

#### 364 **Fibril width range measurements**

365 In all limited-angle tomography experiments (when you cannot tilt through the  
366 entire full range from 0° to 180° or -90° to +90° to collect a full set of projections around  
367 the object of interest), the missing wedge artifact worsens the resolution of raw  
368 tomograms along the Z-axis compared to that in the X and Y directions, often giving the  
369 appearance of elongation of features along the axis with lowest resolution. Therefore,  
370 filament widths cannot be accurately measured in 3D from raw tomograms nor their  
371 corresponding annotations in arbitrary orientations. The most conservative  
372 measurements in the absence of averaging should be performed on slices along the Z-  
373 axis of reconstructed tomograms (*i.e.*, on sections parallel to the XY plane) since features  
374 are much less well-resolved in the XZ and YZ planes. Here, we boxed out filament  
375 segments for STA (below) and manually measured the thinnest and thickest parts of

376 segments (N ~100) from the central XY slice of the corresponding subtomogram. The  
377 mEx1-Q51 and Q51 data were separately processed in identical ways.

### 378 **Initial model generation for subtomogram averaging (STA)**

379 To carry out sub-tiltseries refinement, the new EMAN2 cryoET pipeline<sup>35</sup> requires  
380 that all steps (from initial tomographic reconstruction) be performed in EMAN2. However,  
381 as explained above, whole-tiltseries alignment with IMOD is often superior in quality,  
382 given its refinement of more reconstruction parameters, and reconstruction with ICON-  
383 GPU can yield higher-contrast tomograms with minimized missing wedge artifacts.  
384 Therefore, to generate an initial model, we manually extracted filament segments without  
385 much overlap from the best tomogram for each specimen (n=97 for mEx1-Q51; n=135  
386 for Q51) avoiding branching points and regions of dense bundling or obvious lamination.  
387 Then, we aligned these subtomograms to a cylindrical reference with a soft edge and  
388 computed the average using the legacy tools for STA in EMAN2<sup>77</sup>. This average of  
389 vertically-aligned filaments was then refined constraining the angular search in altitude to  
390 only allow for slightly-tilted orientations (since all particles were already pre-aligned to a  
391 cylinder) and flips of 180° in altitude (the other two Euler angles were completely  
392 unconstrained). Alignment converged in ~4-5 iterations for both datasets. We used these  
393 preliminary averages as initial models for subsequent unconstrained gold-standard  
394 subtomogram averaging of mEx1-Q51 and Q51 with sub-tiltseries refinement in the new  
395 EMAN2 pipeline.

### 396 **Subtomogram averaging**

397 Since the reconstruction geometry is different for tomograms produced with  
398 different software packages, we had to pick subtomograms of filament segments (with <

399 ~50% overlap) manually from scratch (n=450 for mEx1-Q51; n=493 for Q51) in EMAN2-  
400 reconstructed tomograms. Gold-standard refinements seeded with the initial models  
401 described above converged in ~4-5 iteration and ~60% of the best-correlating particles  
402 were kept in the final average for each dataset. The subtiltseries refinement step alone  
403 improved the resolution drastically by ~10 Å or more for both datasets, yielding averages  
404 at ~3.5 nm and ~3.2 nm resolution for mEx1-Q51 and Q51, respectively, according to the  
405 gold-standard FSC=0.143 criterion.

## 406 **Visualization**

407 Tomographic slices were visualized with either EMAN2<sup>37</sup> or IMOD<sup>72</sup>. All  
408 isosurfaces were visualized with UCSF Chimera<sup>78</sup>.

409

## 410 **STATISTICS AND REPRODUCIBILITY**

411 We collected six tomograms of each mEX1-Q51 and Q51 aggregates, and boxed  
412 out 450 and 493 subtomograms of filament segments from each set, respectively, used  
413 for filament width measurements and subtomogram averaging analyses, which are  
414 thoroughly described in the Methods.

415

## 416 **DATA AVAILABILITY AND ACCESSION NUMBERS**

417 The raw data can be made accessible upon request. The Electron Microscopy  
418 Data Bank accession numbers for the structures reported in this paper are as follows:  
419 mEx1-Q51 subtomogram average, EMD-21248; Q51 subtomogram average, EMD-  
420 21253.

421 **AUTHOR CONTRIBUTIONS**

422 All authors planned and designed experiments. K.S. generated and purified the  
423 mEx1-Q51 and Q51 constructs. S.H.S. collected the cryoET data. J.G.G.M. performed all  
424 data processing and analyses, prepared all figures, and wrote the manuscript with  
425 feedback from all authors.

426

427 **ACKNOWLEDGEMENTS AND FUNDING**

428 This research has been supported by grants from the National Institutes of Health,  
429 USA, No. NS092525 to J.F. and W.C., and No. P41GM103832 to W.C.

430

431 **CONFLICTS OF INTEREST DECLARATIONS**

432 The authors declare no conflicts of interest.

433

434 **REPORTING SUMMARY**

435 Further information on research design is available in the Nature Research  
436 Reporting Summary linked to this article.

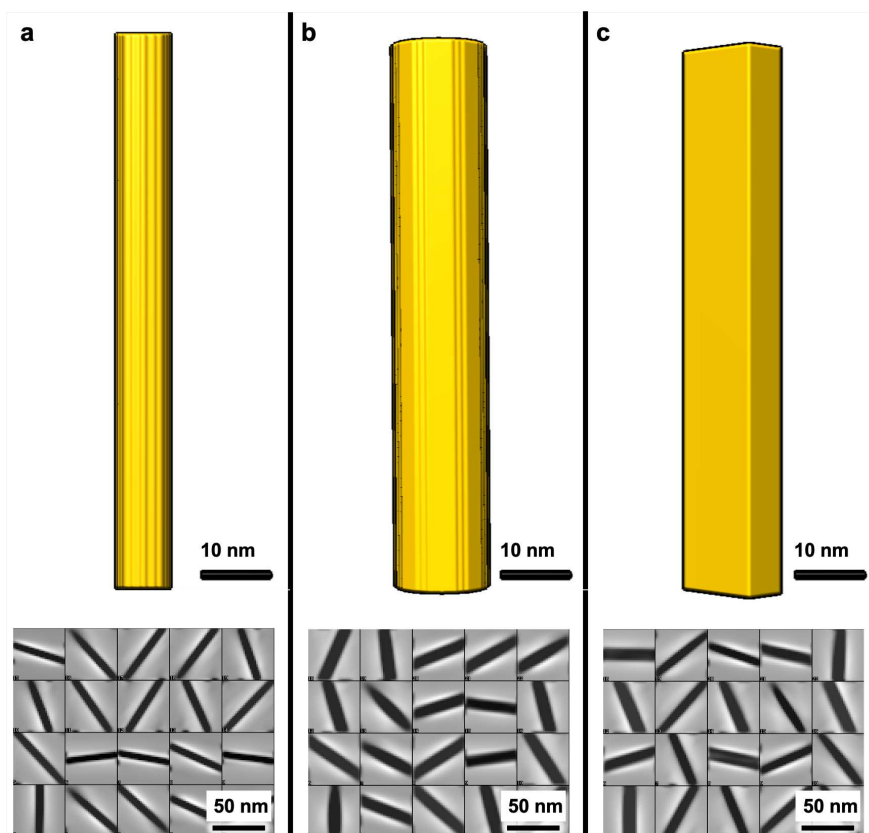
437

438

439

440

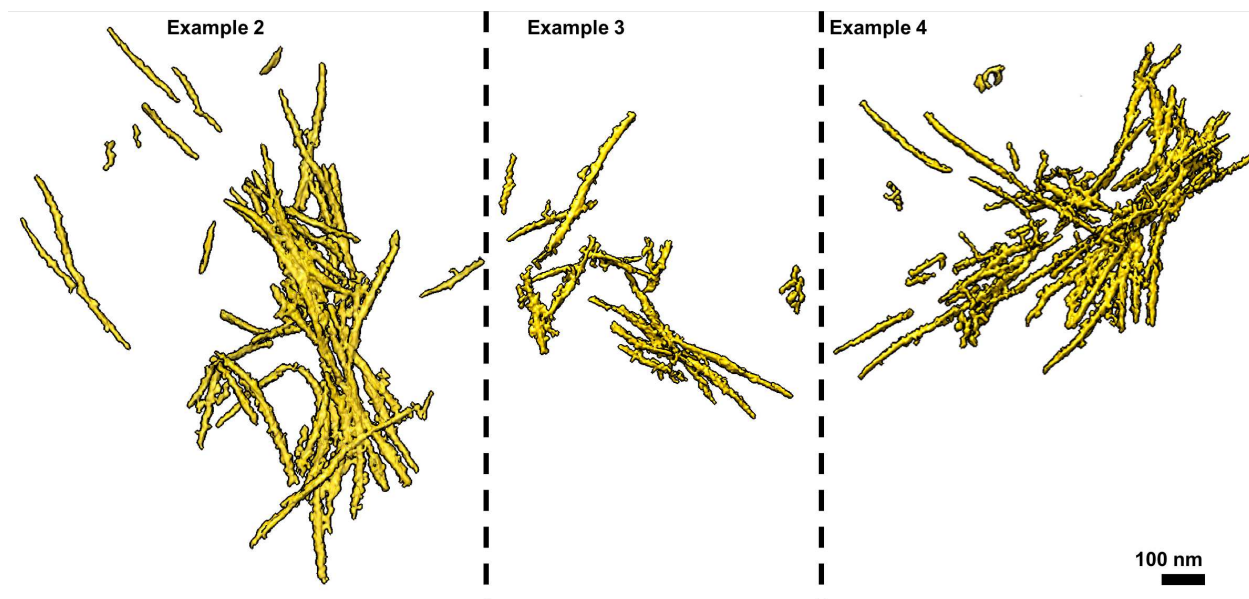
441 **SUPPLEMENTARY DATA**



442

443 **Supplementary Figure S1. Slab-shaped filaments are more consistent with**  
444 **observations of variable width in central Z cross-sections (in the XY plane,**  
445 **unaffected by the missing wedge artifact) than cylindrical filaments. Simulated**  
446 **model and corresponding central Z cross-sections of simulated subtomograms for a**  
447 **cylinder (a) 7 nm or (b) 15 nm in diameter, and (c) a rectangular slab with narrow and**  
448 **wide sides measuring 7 and 15 nm, respectively.**

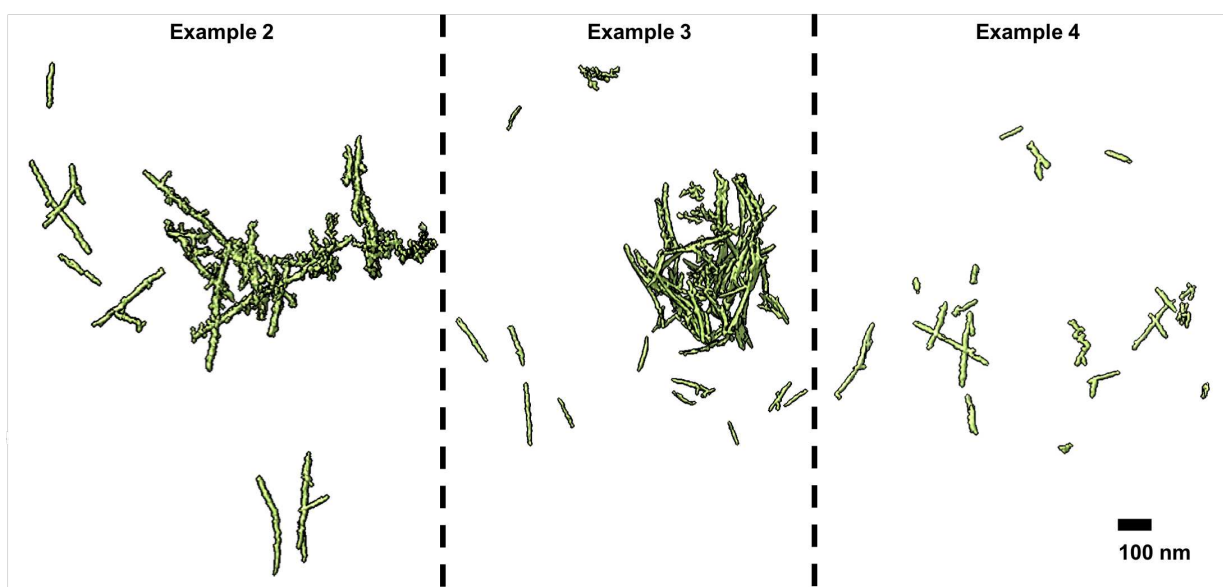
449



450

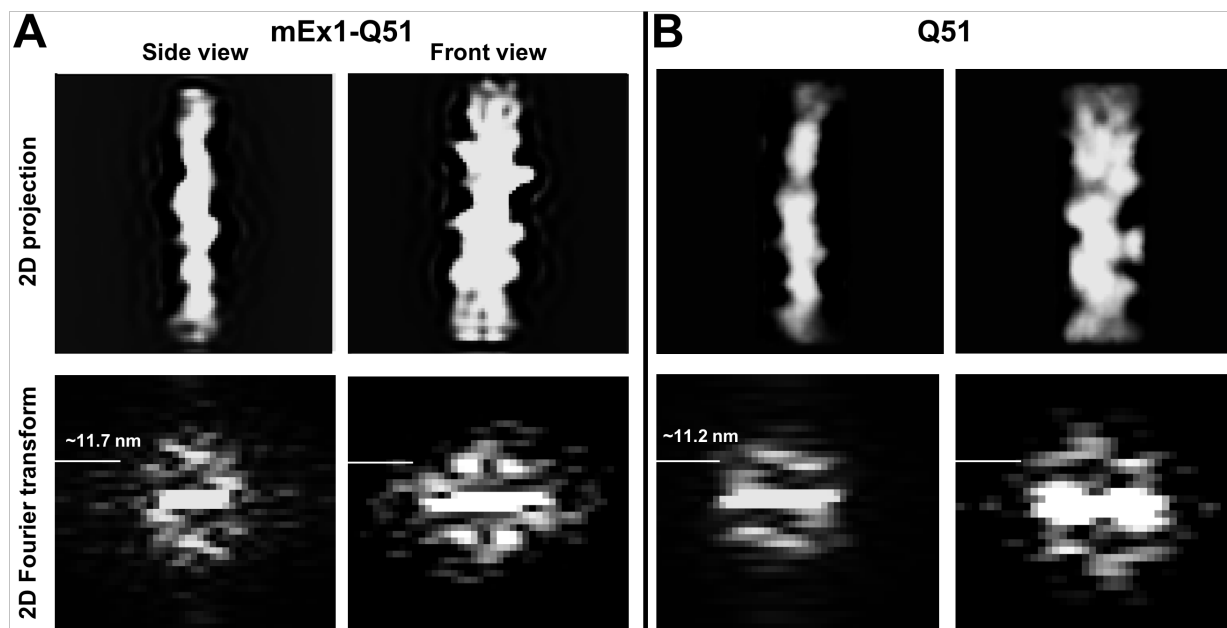
451 **Supplementary Figure S2.** Additional examples of mEx1-Q51 filamentous aggregates.

452



453

454 **Supplementary Figure S3.** Additional examples of Q51 filamentous aggregates.



455

456 **Supplementary Figure S4.** Power spectrum of orthogonal side (left) and face-on (right)  
 457 projections from the subtomogram average of **(a)** mEx1-Q51 (Figure 2C) and **(b)** Q51  
 458 (Figure 4C) filaments.

459

460

461 **REFERENCES**

- 462 1 MacDonald, M. E. *et al.* A novel gene containing a trinucleotide repeat that is  
463 expanded and unstable on Huntington's disease chromosomes. *Cell* **72**, 971-983  
464 (1993).
- 465 2 Testa, C. M. & Jankovic, J. Huntington disease: A quarter century of progress since  
466 the gene discovery. *J Neurol Sci* **396**, 52-68, doi:10.1016/j.jns.2018.09.022 (2019).
- 467 3 Tabrizi, S. J., Ghosh, R. & Leavitt, B. R. Huntingtin Lowering Strategies for Disease  
468 Modification in Huntington's Disease. *Neuron* **101**, 801-819,  
469 doi:10.1016/j.neuron.2019.01.039 (2019).
- 470 4 Wild, E. J. & Tabrizi, S. J. Therapies targeting DNA and RNA in Huntington's  
471 disease. *Lancet Neurol* **16**, 837-847, doi:10.1016/S1474-4422(17)30280-6 (2017).
- 472 5 Mangiarini, L. *et al.* Exon 1 of the HD gene with an expanded CAG repeat is  
473 sufficient to cause a progressive neurological phenotype in transgenic mice. *Cell*  
474 **87**, 493-506, doi:10.1016/s0092-8674(00)81369-0 (1996).
- 475 6 von Hörsten, S. *et al.* Transgenic rat model of Huntington's disease. *Hum Mol*  
476 *Genet* **12**, 617-624, doi:10.1093/hmg/ddg075 (2003).
- 477 7 Wang, L. & Sigworth, F. J. Cryo-EM and single particles. *Physiology* **21**, 13-18  
478 (2006).
- 479 8 Wang, H. *et al.* Suppression of polyglutamine-induced toxicity in cell and animal  
480 models of Huntington's disease by ubiquilin. *Hum Mol Genet* **15**, 1025-1041,  
481 doi:10.1093/hmg/ddl017 (2006).
- 482 9 Yang, S.-H. *et al.* Towards a transgenic model of Huntington's disease in a non-  
483 human primate. *Nature* **453**, 921-924, doi:10.1038/nature06975 (2008).

- 484 10 Davies, S. W. *et al.* Formation of neuronal intranuclear inclusions underlies the  
485 neurological dysfunction in mice transgenic for the HD mutation. *Cell* **90**, 537-548,  
486 doi:10.1016/s0092-8674(00)80513-9 (1997).
- 487 11 DiFiglia, M. *et al.* Aggregation of huntingtin in neuronal intranuclear inclusions and  
488 dystrophic neurites in brain. *Science* **277**, 1990-1993,  
489 doi:10.1126/science.277.5334.1990 (1997).
- 490 12 Sathasivam, K. *et al.* Identical oligomeric and fibrillar structures captured from the  
491 brains of R6/2 and knock-in mouse models of Huntington's disease. *Hum Mol*  
492 *Genet* **19**, 65-78, doi:10.1093/hmg/ddp467 (2010).
- 493 13 Gatchel, J. R. & Zoghbi, H. Y. Diseases of unstable repeat expansion: mechanisms  
494 and common principles. *Nat Rev Genet* **6**, 743-755, doi:10.1038/nrg1691 (2005).
- 495 14 Fan, H.-C. *et al.* Polyglutamine (PolyQ) diseases: genetics to treatments. *Cell*  
496 *Transplant* **23**, 441-458, doi:10.3727/096368914X678454 (2014).
- 497 15 Yang, W., Dunlap, J. R., Andrews, R. B. & Wetzel, R. Aggregated polyglutamine  
498 peptides delivered to nuclei are toxic to mammalian cells. *Hum Mol Genet* **11**,  
499 2905-2917, doi:10.1093/hmg/11.23.2905 (2002).
- 500 16 Redfern, O. C., Dessailly, B. & Orengo, C. A. Exploring the structure and function  
501 paradigm. *Current opinion in structural biology* **18**, 394-402 (2008).
- 502 17 Nekooki-Machida, Y. *et al.* Distinct conformations of in vitro and in vivo amyloids  
503 of huntingtin-exon1 show different cytotoxicity. *Proceedings of the National*  
504 *Academy of Sciences* **106**, 9679-9684 (2009).

- 505 18 Sun, C.-S. *et al.* Conformational switch of polyglutamine-expanded huntingtin into  
506 benign aggregates leads to neuroprotective effect. *Sci Rep* **5**, 14992,  
507 doi:10.1038/srep14992 (2015).
- 508 19 Nucifora, F. C. *et al.* Interference by huntingtin and atrophin-1 with cbp-mediated  
509 transcription leading to cellular toxicity. *Science* **291**, 2423-2428,  
510 doi:10.1126/science.1056784 (2001).
- 511 20 Albin, R. L. Polyglutamine inclusion body toxicity. *Mov Disord* **32**, 1686,  
512 doi:10.1002/mds.27226 (2017).
- 513 21 Scherzinger, E. *et al.* Self-assembly of polyglutamine-containing huntingtin  
514 fragments into amyloid-like fibrils: implications for Huntingtons disease pathology.  
515 *Proceedings of the National Academy of Sciences* **96**, 4604-4609 (1999).
- 516 22 Bugg, C. W., Isas, J. M., Fischer, T., Patterson, P. H. & Langen, R. Structural  
517 features and domain organization of huntingtin fibrils. *J Biol Chem* **287**, 31739-  
518 31746, doi:10.1074/jbc.M112.353839 (2012).
- 519 23 Crick, S. L., Ruff, K. M., Garai, K., Frieden, C. & Pappu, R. V. Unmasking the roles  
520 of N- and C-terminal flanking sequences from exon 1 of huntingtin as modulators  
521 of polyglutamine aggregation. *Proc Natl Acad Sci U S A* **110**, 20075-20080,  
522 doi:10.1073/pnas.1320626110 (2013).
- 523 24 Gruber, A. *et al.* Molecular and structural architecture of polyQ aggregates in yeast.  
524 *Proc Natl Acad Sci U S A* **115**, E3446-E3453, doi:10.1073/pnas.1717978115  
525 (2018).
- 526 25 Bäuerlein, F. J. B. *et al.* In Situ Architecture and Cellular Interactions of PolyQ  
527 Inclusions. *Cell* **171**, 179-187.e110, doi:10.1016/j.cell.2017.08.009 (2017).

528 26 Warner, J. B. *et al.* Monomeric Huntingtin Exon 1 Has Similar Overall Structural  
529 Features for Wild-Type and Pathological Polyglutamine Lengths. *J Am Chem Soc*  
530 **139**, 14456-14469, doi:10.1021/jacs.7b06659 (2017).

531 27 Galaz-Montoya, J. G. & Ludtke, S. J. The advent of structural biology in situ by  
532 single particle cryo-electron tomography. *Biophys Rep* **3**, 17-35,  
533 doi:10.1007/s41048-017-0040-0 (2017).

534 28 Zhang, P. Advances in cryo-electron tomography and subtomogram averaging  
535 and classification. *Curr Opin Struct Biol* **58**, 249-258,  
536 doi:10.1016/j.sbi.2019.05.021 (2019).

537 29 Shahmoradian, S. H. *et al.* TRiCs tricks inhibit huntingtin aggregation. *eLife* **2**,  
538 e00710 (2013).

539 30 Darrow, M. C. *et al.* Structural Mechanisms of Mutant Huntingtin Aggregation  
540 Suppression by the Synthetic Chaperonin-like CCT5 Complex Explained by  
541 Cryoelectron Tomography. *Journal of Biological Chemistry* **290**, 17451-17461  
542 (2015).

543 31 Shen, K. *et al.* Control of the structural landscape and neuronal proteotoxicity of  
544 mutant Huntingtin by domains flanking the polyQ tract. *Elife* **5**,  
545 doi:10.7554/eLife.18065 (2016).

546 32 Deng, Y. *et al.* ICON: 3D reconstruction with 'missing-information' restoration in  
547 biological electron tomography. *Journal of Structural Biology* **195**, 100-112,  
548 doi:10.1016/j.jsb.2016.04.004 (2016).

549 33 Chen, Y. *et al.* Accelerating electron tomography reconstruction algorithm ICON  
550 with GPU. *Biophys Rep* **3**, 36-42, doi:10.1007/s41048-017-0041-z (2017).

551 34 Chen, M. *et al.* Convolutional neural networks for automated annotation of cellular  
552 cryo-electron tomograms. *Nat Methods* **14**, 983-985, doi:10.1038/nmeth.4405  
553 (2017).

554 35 Chen, M. *et al.* A complete data processing workflow for cryo-ET and  
555 subtomogram averaging. *Nat Methods*, doi:10.1038/s41592-019-0591-8 (2019).

556 36 Jin, J. *et al.* Neutralizing Antibodies Inhibit Chikungunya Virus Budding at the  
557 Plasma Membrane. *Cell Host Microbe* **24**, 417-428.e415,  
558 doi:10.1016/j.chom.2018.07.018 (2018).

559 37 Galaz-Montoya, J. G., Flanagan, J., Schmid, M. F. & Ludtke, S. J. Single particle  
560 tomography in EMAN2. *Journal of structural biology* **190**, 279-290 (2015).

561 38 Dobson, C. M. The structural basis of protein folding and its links with human  
562 disease. *Philos Trans R Soc Lond B Biol Sci* **356**, 133-145,  
563 doi:10.1098/rstb.2000.0758 (2001).

564 39 Maiuri, T., Woloshansky, T., Xia, J. & Truant, R. The huntingtin N17 domain is a  
565 multifunctional CRM1 and Ran-dependent nuclear and cilial export signal. *Hum*  
566 *Mol Genet* **22**, 1383-1394, doi:10.1093/hmg/dds554 (2013).

567 40 Scherzinger, E. *et al.* Huntingtin-encoded polyglutamine expansions form amyloid-  
568 like protein aggregates in vitro and in vivo. *Cell* **90**, 549-558, doi:10.1016/s0092-  
569 8674(00)80514-0 (1997).

570 41 Chen, S., Berthelie, V., Yang, W. & Wetzel, R. Polyglutamine aggregation  
571 behavior in vitro supports a recruitment mechanism of cytotoxicity. *J Mol Biol* **311**,  
572 173-182, doi:10.1006/jmbi.2001.4850 (2001).

573 42 Chen, S., Berthelier, V., Hamilton, J. B., O'Nuallain, B. & Wetzel, R. Amyloid-like  
574 features of polyglutamine aggregates and their assembly kinetics. *Biochemistry*  
575 **41**, 7391-7399, doi:10.1021/bi011772q (2002).

576 43 Fitzpatrick, A. W. P. *et al.* Cryo-EM structures of tau filaments from Alzheimer's  
577 disease. *Nature* **547**, 185-190, doi:10.1038/nature23002 (2017).

578 44 Gremer, L. *et al.* Fibril structure of amyloid-beta(1-42) by cryo-electron microscopy.  
579 *Science* **358**, 116-119, doi:10.1126/science.aao2825 (2017).

580 45 Guerrero-Ferreira, R. *et al.* Cryo-EM structure of alpha-synuclein fibrils. *Elife* **7**,  
581 doi:10.7554/eLife.36402 (2018).

582 46 Li, B. *et al.* Cryo-EM of full-length alpha-synuclein reveals fibril polymorphs with a  
583 common structural kernel. *Nat Commun* **9**, 3609, doi:10.1038/s41467-018-05971-  
584 2 (2018).

585 47 Li, Y. *et al.* Amyloid fibril structure of alpha-synuclein determined by cryo-electron  
586 microscopy. *Cell Res* **28**, 897-903, doi:10.1038/s41422-018-0075-x (2018).

587 48 Iadanza, M. G., Jackson, M. P., Hewitt, E. W., Ranson, N. A. & Radford, S. E. A  
588 new era for understanding amyloid structures and disease. *Nat Rev Mol Cell Biol*  
589 **19**, 755-773, doi:10.1038/s41580-018-0060-8 (2018).

590 49 Fitzpatrick, A. W. & Saibil, H. R. Cryo-EM of amyloid fibrils and cellular aggregates.  
591 *Curr Opin Struct Biol* **58**, 34-42, doi:10.1016/j.sbi.2019.05.003 (2019).

592 50 Scheres, S. H., Zhang, W., Falcon, B. & Goedert, M. Cryo-EM structures of tau  
593 filaments. *Curr Opin Struct Biol* **64**, 17-25, doi:10.1016/j.sbi.2020.05.011 (2020).

594 51 Wetzel, R. Physical chemistry of polyglutamine: intriguing tales of a monotonous  
595 sequence. *J Mol Biol* **421**, 466-490, doi:10.1016/j.jmb.2012.01.030 (2012).

596 52 Ruggeri, F. S. *et al.* Nanoscale studies link amyloid maturity with polyglutamine  
597 diseases onset. *Sci Rep* **6**, 31155, doi:10.1038/srep31155 (2016).

598 53 Jensen, E. C. Use of fluorescent probes: their effect on cell biology and limitations.  
599 *Anat Rec (Hoboken)* **295**, 2031-2036, doi:10.1002/ar.22602 (2012).

600 54 Rigort, A. *et al.* Automated segmentation of electron tomograms for a quantitative  
601 description of actin filament networks. *J Struct Biol* **177**, 135-144,  
602 doi:10.1016/j.jsb.2011.08.012 (2012).

603 55 Rusu, M., Starosolski, Z., Wahle, M., Rigort, A. & Wriggers, W. Automated tracing  
604 of filaments in 3D electron tomography reconstructions using Sculptor and Situs.  
605 *J Struct Biol* **178**, 121-128, doi:10.1016/j.jsb.2012.03.001 (2012).

606 56 Yu, Z. & Frangakis, A. S. M-free: scoring the reference bias in sub-tomogram  
607 averaging and template matching. *J Struct Biol* **187**, 10-19,  
608 doi:10.1016/j.jsb.2014.05.007 (2014).

609 57 Hecksel, C. W. *et al.* Quantifying Variability of Manual Annotation in Cryo-Electron  
610 Tomograms. *Microscopy and microanalysis: the official journal of Microscopy*  
611 *Society of America, Microbeam Analysis Society, Microscopical Society of*  
612 *Canada*, 1-10 (2016).

613 58 Wagner, A. S. *et al.* Self-assembly of Mutant Huntingtin Exon-1 Fragments into  
614 Large Complex Fibrillar Structures Involves Nucleated Branching. *J Mol Biol* **430**,  
615 1725-1744, doi:10.1016/j.jmb.2018.03.017 (2018).

616 59 Lu, K., Jacob, J., Thiyagarajan, P., Conticello, V. P. & Lynn, D. G. Exploiting  
617 amyloid fibril lamination for nanotube self-assembly. *J Am Chem Soc* **125**, 6391-  
618 6393, doi:10.1021/ja0341642 (2003).

619 60 Poirier, M. A. *et al.* Huntingtin spheroids and protofibrils as precursors in  
620 polyglutamine fibrilization. *J Biol Chem* **277**, 41032-41037,  
621 doi:10.1074/jbc.M205809200 (2002).

622 61 Schneider, R. *et al.* Structural characterization of polyglutamine fibrils by solid-  
623 state NMR spectroscopy. *J Mol Biol* **412**, 121-136, doi:10.1016/j.jmb.2011.06.045  
624 (2011).

625 62 Duim, W. C., Chen, B., Frydman, J. & Moerner, W. E. Sub-diffraction imaging of  
626 huntingtin protein aggregates by fluorescence blink-microscopy and atomic force  
627 microscopy. *Chemphyschem* **12**, 2387-2390, doi:10.1002/cphc.201100392  
628 (2011).

629 63 Duim, W. C., Jiang, Y., Shen, K., Frydman, J. & Moerner, W. E. Super-resolution  
630 fluorescence of huntingtin reveals growth of globular species into short fibers and  
631 coexistence of distinct aggregates. *ACS Chem Biol* **9**, 2767-2778,  
632 doi:10.1021/cb500335w (2014).

633 64 Sivanandam, V. N. *et al.* The aggregation-enhancing huntingtin N-terminus is  
634 helical in amyloid fibrils. *J Am Chem Soc* **133**, 4558-4566, doi:10.1021/ja110715f  
635 (2011).

636 65 Hoop, C. L. *et al.* Polyglutamine amyloid core boundaries and flanking domain  
637 dynamics in huntingtin fragment fibrils determined by solid-state nuclear magnetic  
638 resonance. *Biochemistry* **53**, 6653-6666, doi:10.1021/bi501010q (2014).

639 66 Hoop, C. L. *et al.* Huntingtin exon 1 fibrils feature an interdigitated  $\beta$ -hairpin-based  
640 polyglutamine core. *Proc Natl Acad Sci U S A* **113**, 1546-1551,  
641 doi:10.1073/pnas.1521933113 (2016).

642 67 Lin, H.-K. *et al.* Fibril polymorphism affects immobilized non-amyloid flanking  
643 domains of huntingtin exon1 rather than its polyglutamine core. *Nat Commun* **8**,  
644 15462, doi:10.1038/ncomms15462 (2017).

645 68 Vieweg, S., Ansaloni, A., Wang, Z. M., Warner, J. B. & Lashuel, H. A. An Intein-  
646 based Strategy for the Production of Tag-free Huntingtin Exon 1 Proteins Enables  
647 New Insights into the Polyglutamine Dependence of Httex1 Aggregation and Fibril  
648 Formation. *J Biol Chem* **291**, 12074-12086, doi:10.1074/jbc.M116.713982 (2016).

649 69 Adegbuyiro, A., Sedighi, F., Pilkington, A. W. t., Groover, S. & Legleiter, J. Proteins  
650 Containing Expanded Polyglutamine Tracts and Neurodegenerative Disease.  
651 *Biochemistry* **56**, 1199-1217, doi:10.1021/acs.biochem.6b00936 (2017).

652 70 Hegde, R. N. *et al.* TBK1 phosphorylates mutant Huntingtin and suppresses its  
653 aggregation and toxicity in Huntington's disease models. *EMBO J* **39**, e104671,  
654 doi:10.15252/embj.2020104671 (2020).

655 71 Mastronarde, D. N. Automated electron microscope tomography using robust  
656 prediction of specimen movements. *Journal of structural biology* **152**, 36-51  
657 (2005).

658 72 Kremer, J. R., Mastronarde, D. N. & McIntosh, J. R. Computer visualization of  
659 three-dimensional image data using IMOD. *Journal of structural biology* **116**, 71-  
660 76 (1996).

661 73 Radermacher, M. Three-Dimensional reconstruction of single particles from  
662 random and nonrandom tilt series. *Journal of Electron Microscopy Technique* **9**,  
663 359-394 (1988).

664 74 Iwasaki, K. *et al.* Electron tomography reveals diverse conformations of integrin  
665  $\alpha$ IIb $\beta$ 3 in the active state. *Journal of structural biology* **150**, 259-267 (2005).

666 75 Bartesaghi, A. *et al.* Classification and 3D averaging with missing wedge correction  
667 in biological electron tomography. *Journal of structural biology* **162**, 436-450  
668 (2008).

669 76 Zhang, L. & Ren, G. IPET and FETR: experimental approach for studying  
670 molecular structure dynamics by cryo-electron tomography of a single-molecule  
671 structure. *PloS one* **7**, e30249, doi:10.1371/journal.pone.0030249 (2012).

672 77 Galaz-Montoya, J. G. *et al.* Alignment algorithms and per-particle CTF correction  
673 for single particle cryo-electron tomography. *Journal of structural biology* **194**, 383-  
674 394 (2016).

675 78 Pettersen, E. F. *et al.* UCSF Chimera--a visualization system for exploratory  
676 research and analysis. *J Comput Chem* **25**, 1605-1612, doi:10.1002/jcc.20084  
677 (2004).

678

# Figures

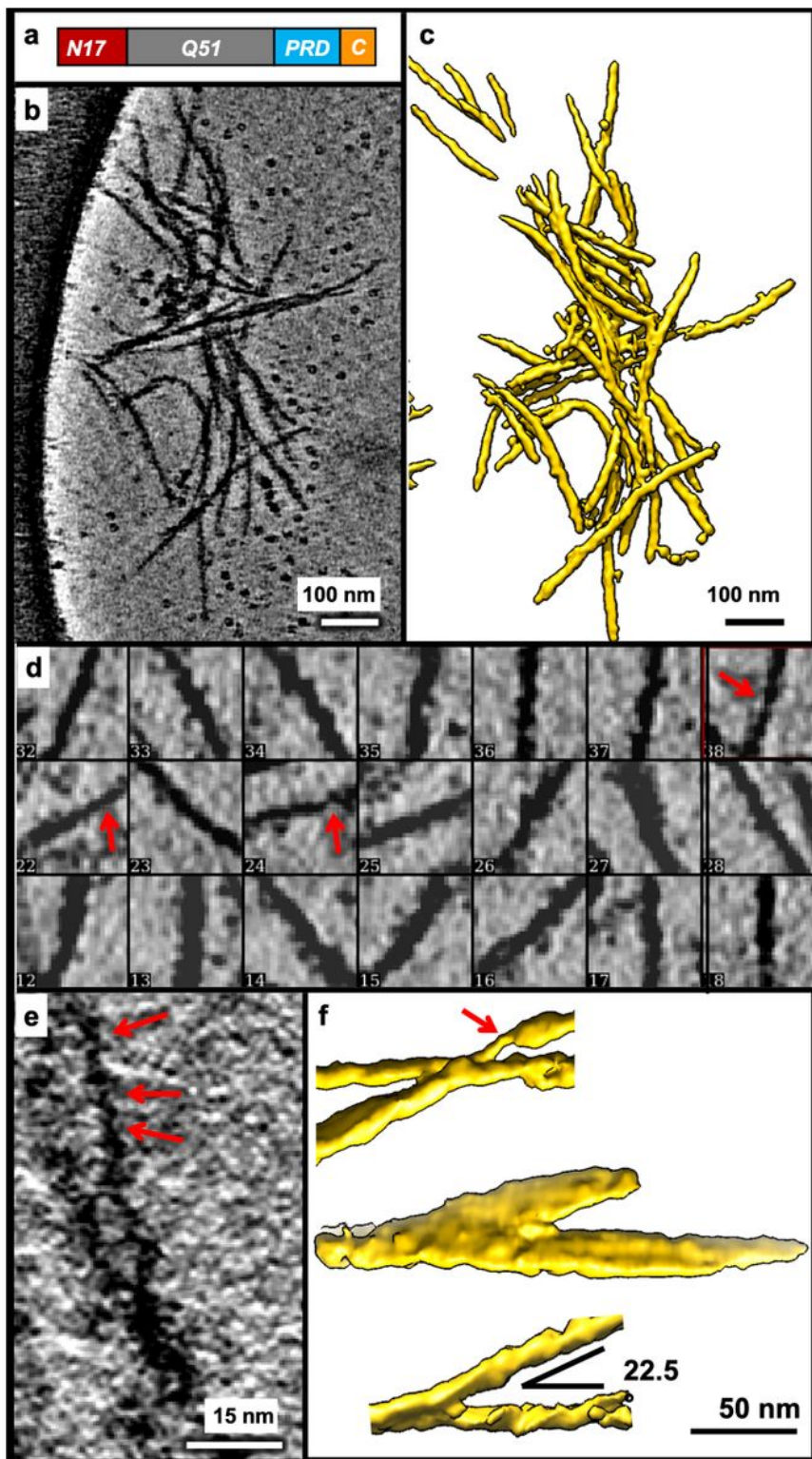
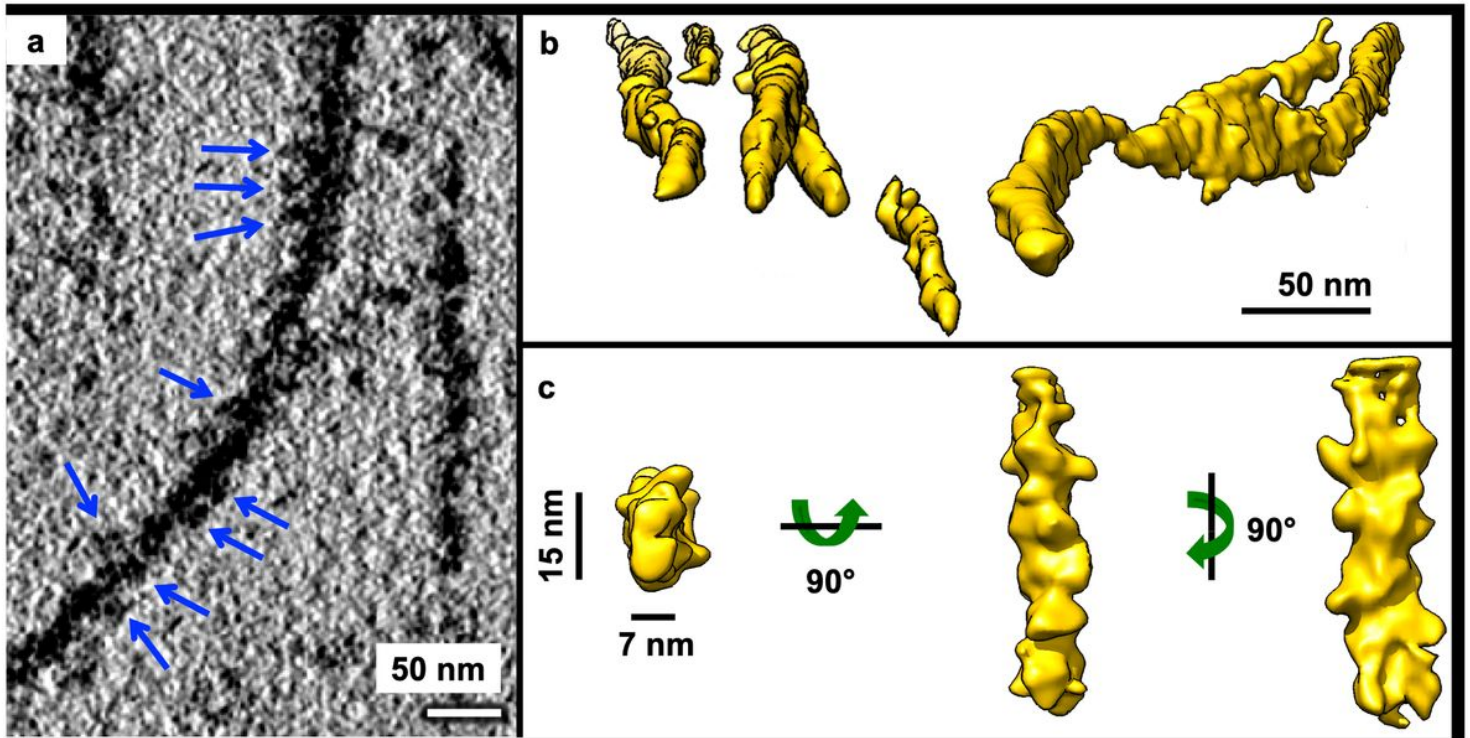


Figure 1

mEx1-Q51 filaments exhibit a large variation in width within and across filaments. (a) Schematic of the mEx1-Q51 construct. (b) Slice parallel to xy ( $\sim 1.7$  nm thick) through a representative 4x down-sampled cryoET tomogram of aggregated mEx1-Q51, reconstructed with compressed sensing, lightly filtered to

enhance visualization, and (c) corresponding semi-automated 3D annotation. (d) Selected areas from slices of large mEx1-Q51 aggregates showing individual filaments, widely varying in width, with the thinnest filaments exhibiting regions down to  $\sim 2$  nm width, indicated by the redarrows. (e) Zoomed-in view of a xy slice ( $\sim 0.4$  nm thick) from a selected region of a tomogram without any down-sampling, showcasing ultra-thin regions in mEx1-Q51 filaments. (f) Sections of annotated mEX1- Q51 filamentous aggregates from cryoET tomograms showing relatively narrow branching angles and an example of a thicker laminated sheet-like region (the annotation example in the middle).



**Figure 2**

Aggregated mEx1-Q51 exhibits lumpy, slab-shaped filaments. (a) Pseudo periodic pattern of repeating lumps (blue arrows) along the length of an mEx1-Q51 filament as seen in an xy slice ( $4.4 \text{ \AA}$  thick) from a tomogram of aggregated mEx1-Q51. (b) Selected regions from semi-automated neural network annotations showing lumpy filaments of various widths, including sheet-like regions (middle region of right-most example). (c) Subtomogram average of a subpopulation of filament segments exhibiting a lumpy  $7 \times 15$  nm slab-shaped morphology.

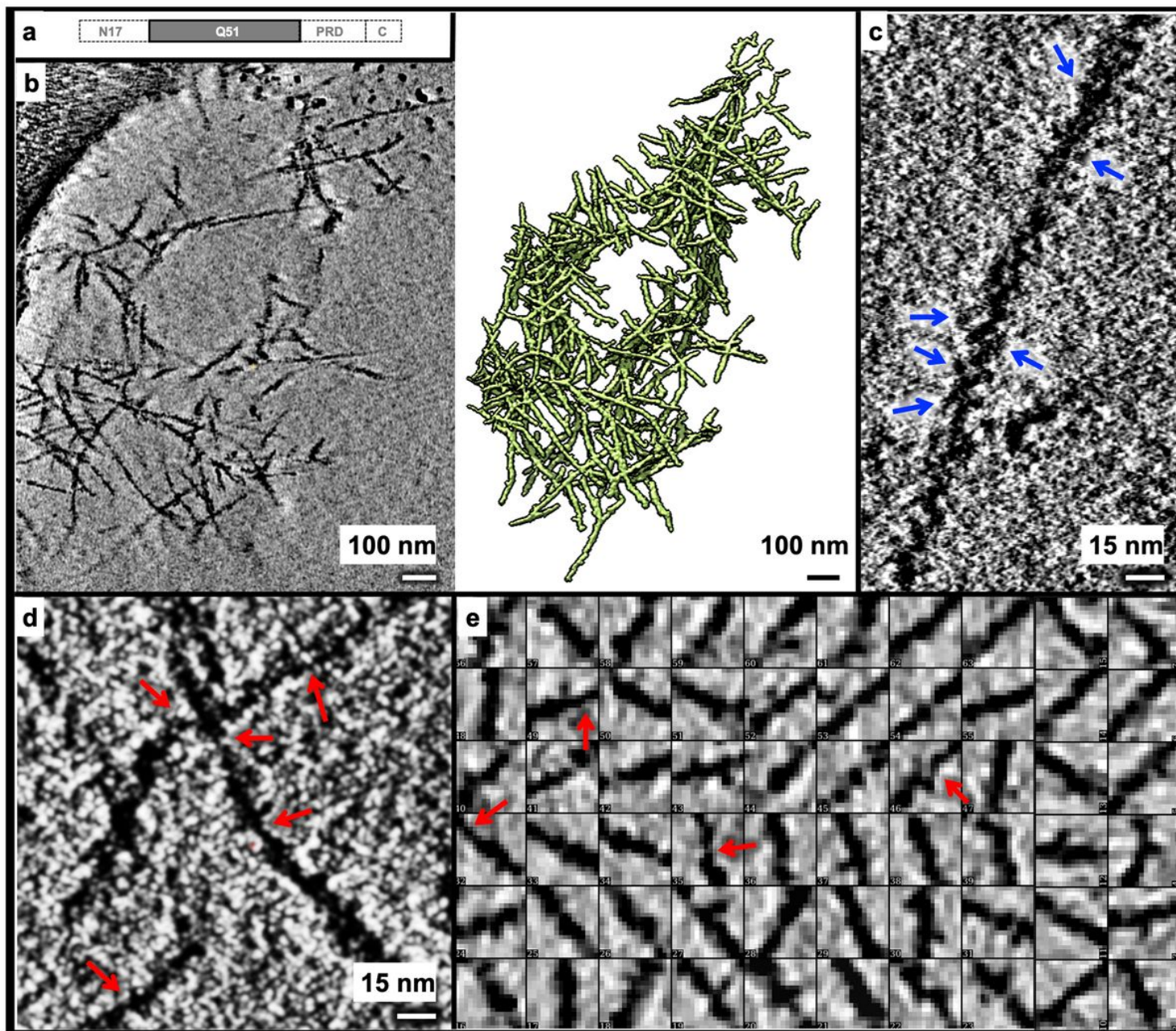


**Figure 3**

Lumpy Q51 filaments exhibit a large range of widths. (a) Schematic of the Q51 construct, lacking all mEx1 domains except for the polyQ tract. (b) Slice parallel to the xy plane ( $\sim 2.1$  nm thick) through a representative 4x down-sampled cryoET tomogram of aggregated Q51 reconstructed with compressed sensing (left) and corresponding 3D annotation (right). Zoomed-in views of xy slices ( $\sim 0.5$  nm thick) from selected regions of the tomogram shown in A but without any down-sampling, exhibiting (c) a pseudo periodic pattern of repeating lumps along the length of a Q51 filament (blue arrows), and (d) regions in thin filaments that are as thin as  $\sim 2$  nm in width (red arrows). (e) Examples of 2D xy slices through representative 3D subtomograms of Q51 filaments showing a wide variation in width, including super-thin regions  $\sim 2$  nm in width (red arrows).

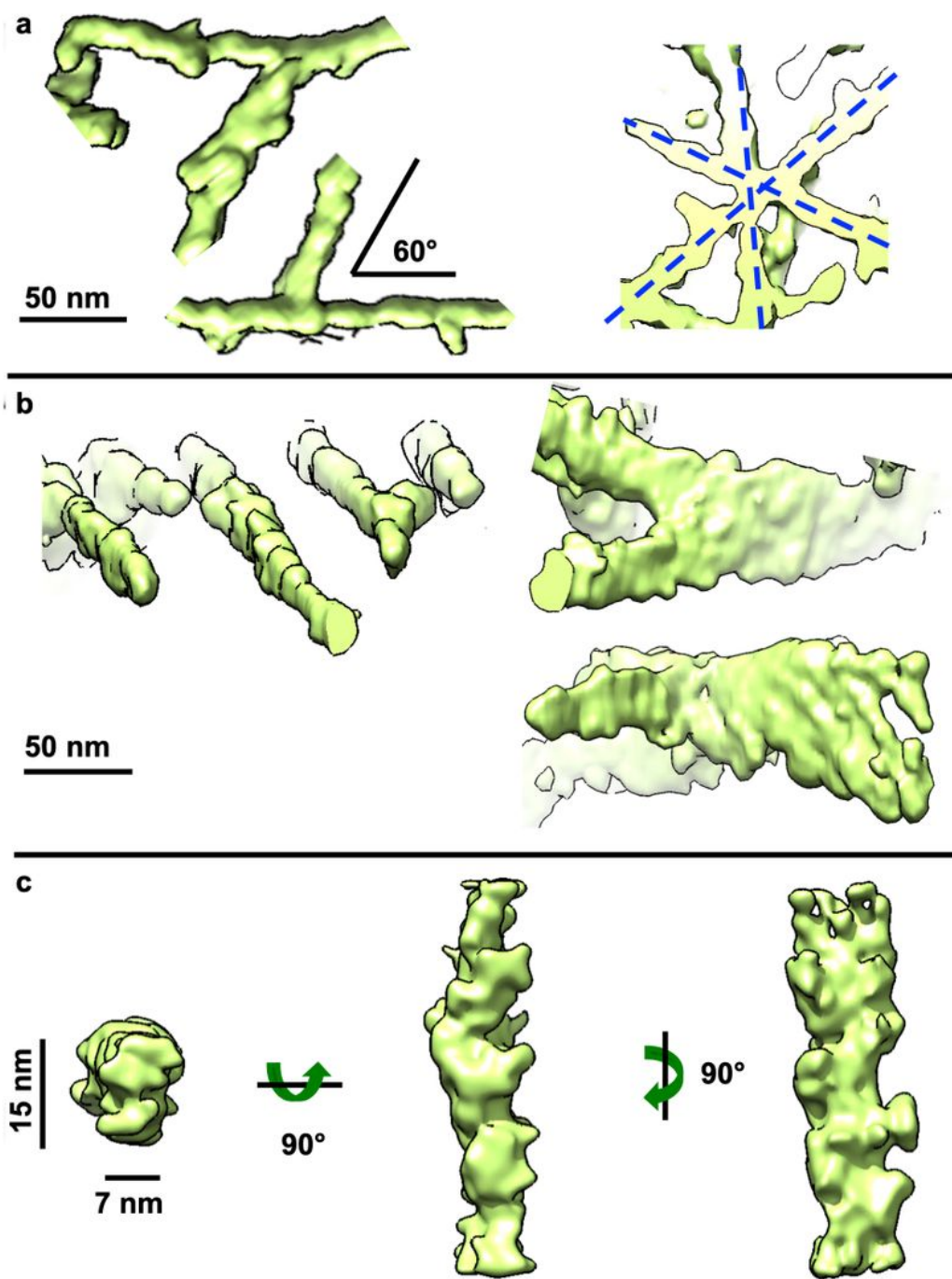


**Figure 4**

Aggregated Q51 exhibits lamination sheets and predominantly lumpy, slab-shaped filaments. (a) Representative sections of annotated Q51 filamentous aggregates from cryoET tomograms showing their most common branching/crossover angle ( $\sim 60^\circ$ ), often in an asterisk like pattern, and (b) thicker regions (right) akin to lamination, onside thinner ones (left). (c) Subtomogram average of a subpopulation of filament segments exhibiting a lumpy 7x15 nm slab-shaped morphology.

## Supplementary Files

This is a list of supplementary files associated with this preprint. Click to download.

- [rs.pdf](#)